Sulfur Vacancy-Carbon Modification Synergy Boosts Electrochemical Performance of Self-Standing VS_2 Cathodes in Aqueous Zinc-Ion Batteries

*Dongxu Wu,[‡a] Zihao Jie,[‡a] Yong Wei,[a] Linfeng Zhong,[a] Yingqi Zhang,[a] Qi Cheng,[a] Ming Jiang,[*a] Chuanqiang Wu[*a]*

[a] Information Materials and Intelligent Sensing Laboratory of Anhui Province, Institutes of Physical Science and Information Technology, Anhui University, Hefei 230601, China.

Corresponding Author

*Email: Wucq@ahu.edu.cn (C. W)

[‡] They contributed equally.

Experimental Procedures

The C-VS_2 nanosheets grown on stainless steel mesh (SSM) were synthesized via a hydrothermal method. Briefly, 0.132 mmol of ammonium metavanadate (NH_4VO_3) and 0.61 mmol of glucose were sequentially dissolved in 18 mL of deionized water (DIW), followed by stirring for 30 min. Subsequently, 1 mmol of thioacetamide (TAA) and 1.32 mL of ammonia solution (NH_3H_2O) were added to the homogeneous mixture, and the resulting solution was subjected to continuous magnetic stirring at room temperature for 1 h to form a uniform black suspension. The 500-mesh SSM was cut into circular discs with a diameter of 16 mm, which were ultrasonically cleaned in acetone, absolute ethanol, and DIW for 15 min each, and finally dried in a freeze dryer. The pretreated SSM discs were immersed into the as-prepared black suspension, and the mixture was transferred into a 25 mL stainless steel autoclave. The autoclave was sealed and heated in a blast drying oven at 190 °C for different durations (5 h, 10 h, 18 h, and 20 h). After naturally cooling down to room temperature, the autoclave was opened, and the SSM samples were rinsed alternately with DIW and absolute ethanol several times. The obtained products were dried overnight at 70 °C in a vacuum drying oven, yielding the self-supported C-VS_2@SS composites. For comparison, C-VS_2, VS_2@SS, and pristine VS_2 were synthesized via the same hydrothermal protocol with the absence of SSM, glucose, or both, respectively.

Material Characterization

Powder X-ray diffraction (XRD) measurements were performed on a Philips X'Pert Pro Super diffractometer equipped with Cu K_α radiation (λ=1.54178 nm). The diffraction patterns were collected over a 2θ range of 10°-90° at a scanning rate of $2°min^{-1}$. The morphological features of the samples were characterized using a Carl Zeiss Crossbeam 550 focused ion beam scanning electron microscope (FIB-SEM). The microstructure and chemical composition were analyzed by transmission electron microscopy (TEM, JEOL-F200) and energy-dispersive X-ray spectroscopy (EDS). High-angle annular dark-field scanning transmission electron microscopy (HAADF-STEM) measurements using a 200 kV JEM-ARM200F equipped with single spherical aberration correctors. Raman spectra were recorded on an in Via-Reflex confocal

Raman spectrometer with a 532 nm laser excitation source. Fourier-transform infrared (FTIR) spectra were obtained using a Vertex80+Hyperion2000 spectrometer. X-ray photoelectron spectroscopy (XPS) measurements were carried out on a VG ESCALAB MK II spectrometer with an Mg K_α X-ray source (hv=1253.6 eV). All the binding energies in the XPS spectra were calibrated against the C 1s peak at 284.5 eV to eliminate the charging effect of the samples.

Electrochemical Measurements

For the self-supported C-VS_2@SS and VS_2@SS electrodes, they were directly used as cathodes without any additional coating process. CR2032-type coin cells were assembled in ambient air using zinc foil as the anode, glass fiber membrane as the separator, and 2 M zinc sulfate ($ZnSO_4$) aqueous solution as the electrolyte. For C-VS_2 and pristine VS_2, the cathode electrodes were prepared via a conventional slurry-coating method. Typically, the active materials (C-VS_2 or VS_2, 70 wt%), Ketjen Black (20 wt%), and polyvinylidene fluoride (PVDF, 10 wt%) were thoroughly ground in an agate mortar, followed by the addition of N-methylpyrrolidone (NMP) to form a homogeneous slurry. The slurry was uniformly coated onto 500-mesh 316L SSM discs (16 mm in diameter) and dried overnight at 70 °C in a vacuum drying oven. The assembly of coin cells followed the same procedure as described above. The electrochemical performances of the assembled cells were tested on a LAND battery test system (CT2001A) within a voltage window of 0.4-1 V. Cyclic voltammetry (CV) and electrochemical impedance spectroscopy (EIS) measurements were conducted on a CHI600E electrochemical workstation. All the tests were performed at room temperature.

Computational details

All of the calculations were performed in the framework of the spin-polarized density functional theory with the projector augmented plane-wave method, as implemented in the Vienna ab initio simulation package (VASP) code [1, 2]. The projector augmented-wave (PAW) pseudopotentials [3] were employed to describe the interaction between ions and electrons, and the exchange-correlation potential was described by Perdew-Burke-Ernzerhof (PBE) functional within the generalized gradient approximation

(GGA)[4]. The valence electronic configurations for PAW pseudopotentials are $3d^4 4s^1$ for V, $3s^2 3p^4$ for S, $2s^2 2p^2$ for C and $3d^{10} 4p^2$ for Zn. To explore the adsorption and migration behaviors of Zn^{2+}, the C-VS_2 heterostructure was built, and a vacuum spacing of 15 Å is applied perpendicular to the slab to avoid interlaminar interactions. Atomic visualization was carried out with the help of VESTA. The long-range van der Waals interaction is described by the DFT-D3 approach [5]. A cut-off energy of 500 eV and a k-point sampling of were selected. The convergence criteria for total energies and forces were set to 10^{-6} eV and 10^{-2} eV/Å, respectively. The diffusion barrier at different adsorption sites were explored by using the Nudge Elastic Band (CI-NEB) method.

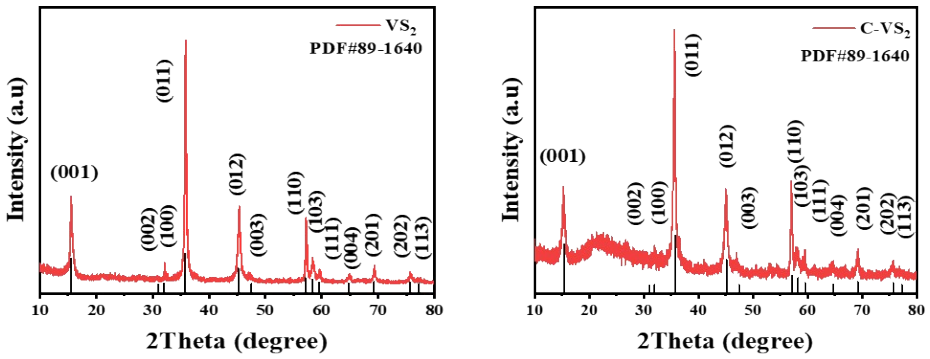

Figure S1. XRD patterns of C-$VS_2$and VS_2.

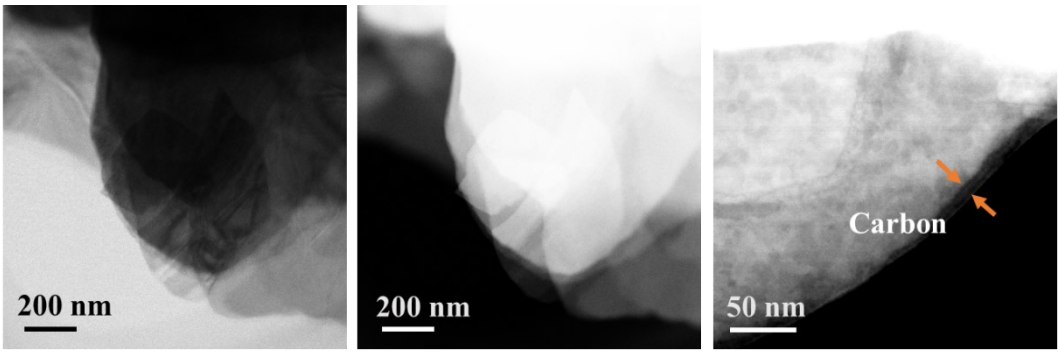

Figure S2. ABF-STEM and HAADF-STEM micrographs of C-VS_2@SS.

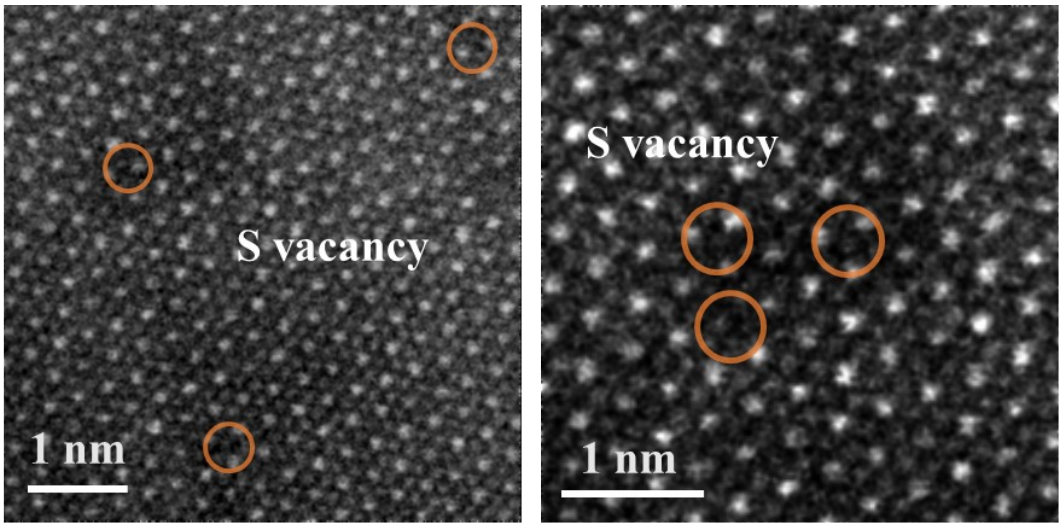

Figure S3. HAADF-STEM micrographs of C-VS_2@SS.

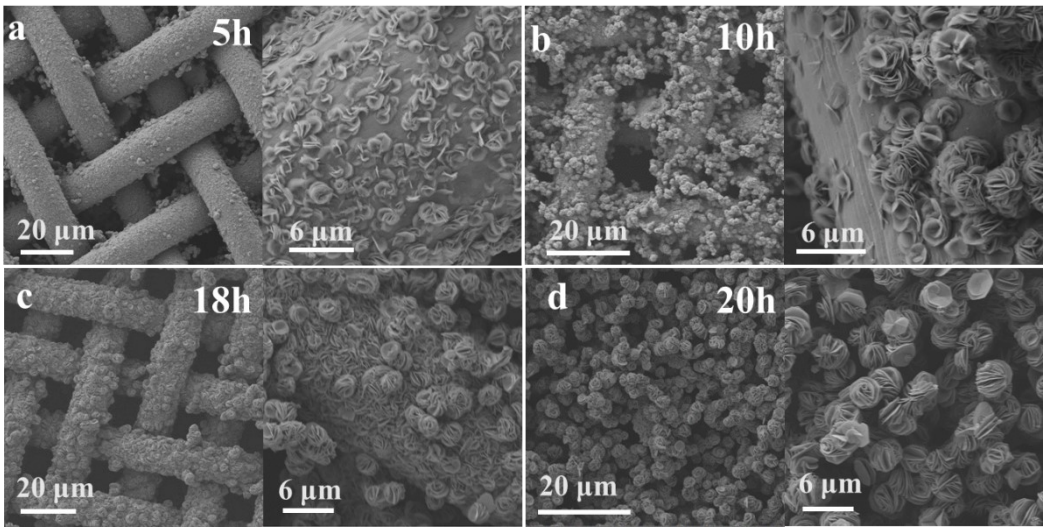

Figure S4. SEM images of C-VS_2@SS synthesized at hydrothermal durations of 5 h, 10 h, 18 h and 20 h.

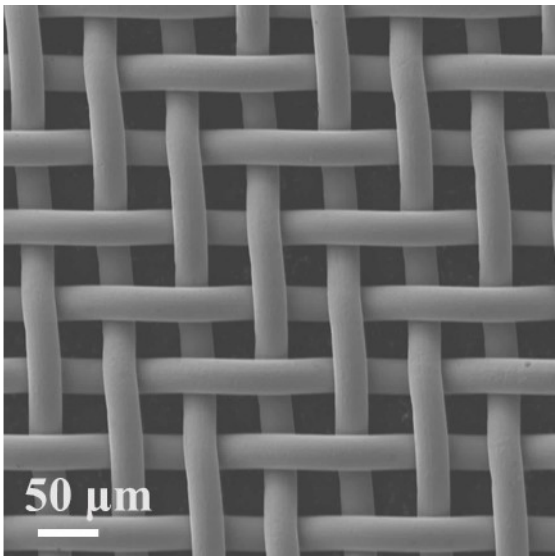

Figure S5. SEM micrographs of unloaded stainless steel mesh.

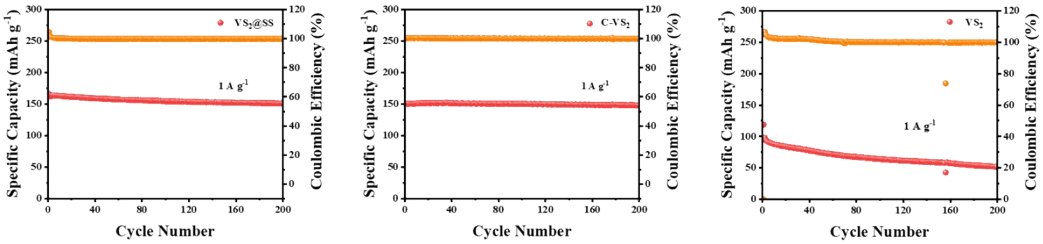

Figure S6. Cycling performance of VS_2@SS, C-VS_2 and VS_2 at a current density of 1 A g^{-1}.

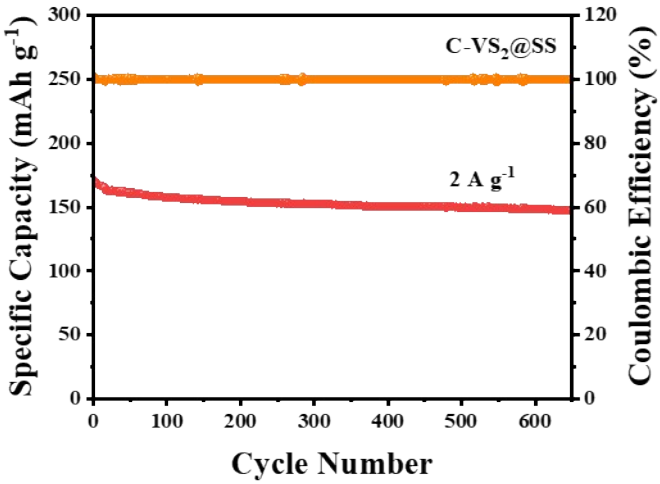

Figure S7. Cycling performance of C-VS_2@SS at a current density of 2 A g^{-1}.

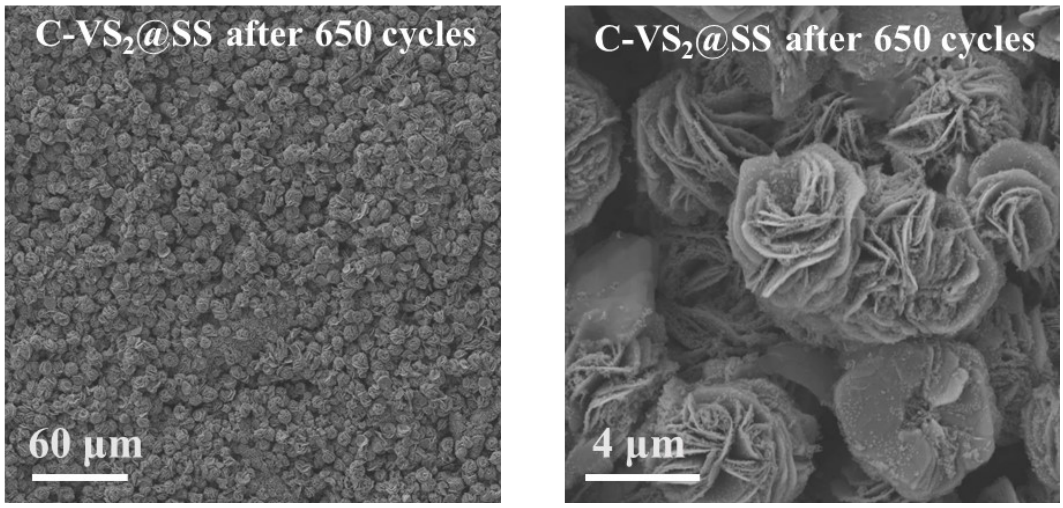

Figure S8. SEM micrographs of C-VS_2@SS after 650 cycles at a current density of 2 A g^{-1}.

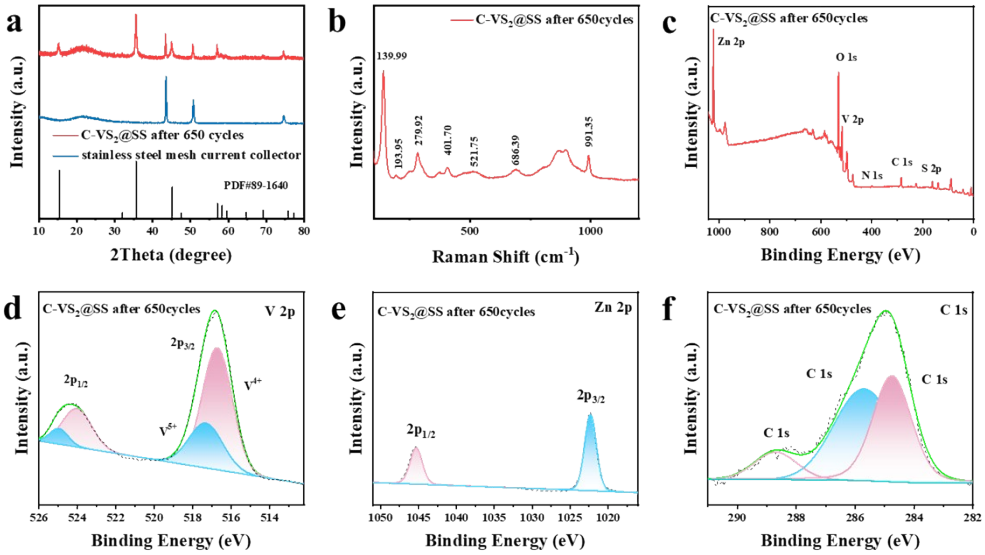

Figure S9. XRD (a), Raman (b) and XPS (c-f) patterns of C-VS_2@SS after 650 cycles at a current density of 2 A g^{-1}.

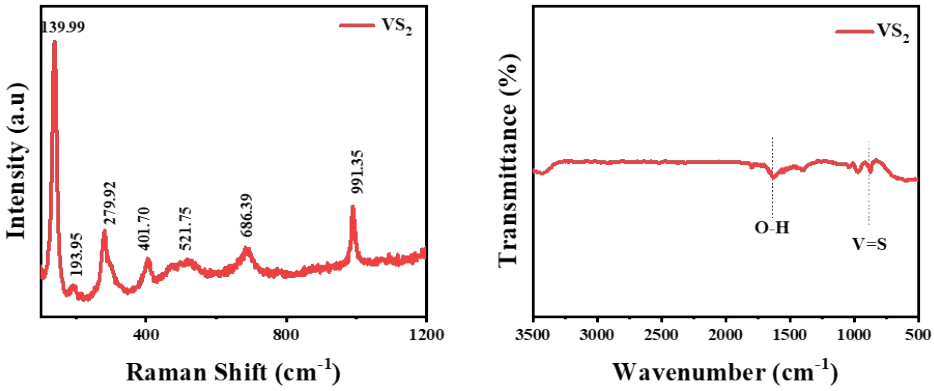

Figure S10. Raman and FTIR spectra of VS_2.

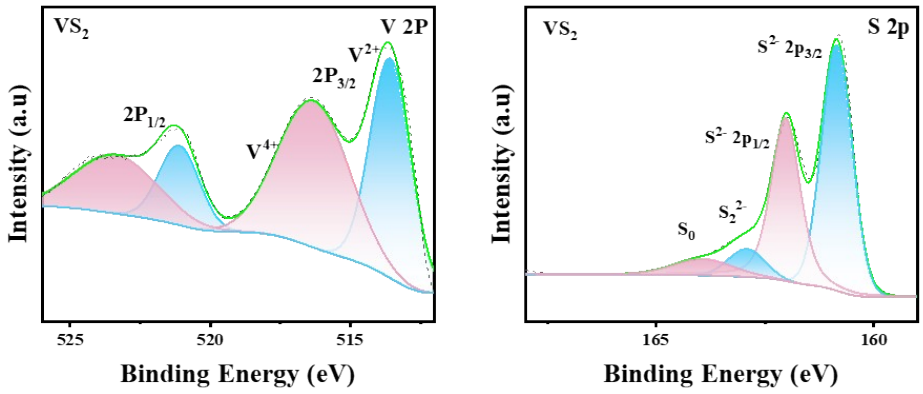

Figure S11. V 2p, S 2p, XPS spectra of VS_2.

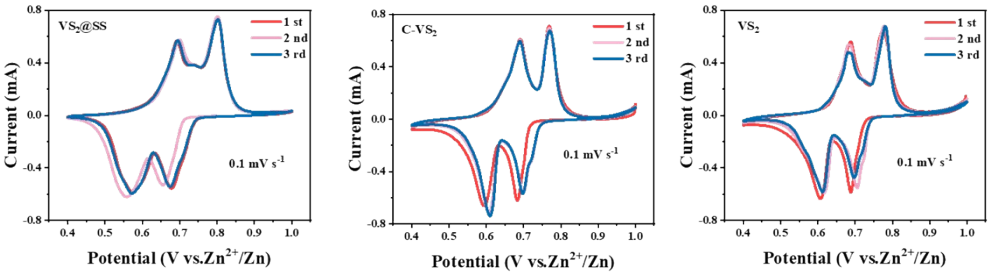

Figure S12. CV spectra of VS_2@SS, C-VS_2 and VS_2 at a scan rate of 0.1 mV s^{-1}.

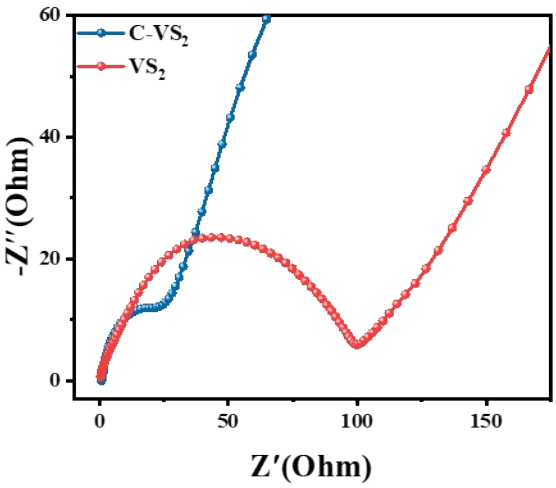

Figure S13. EIS Nyquist plots of C-VS_2 and VS_2.

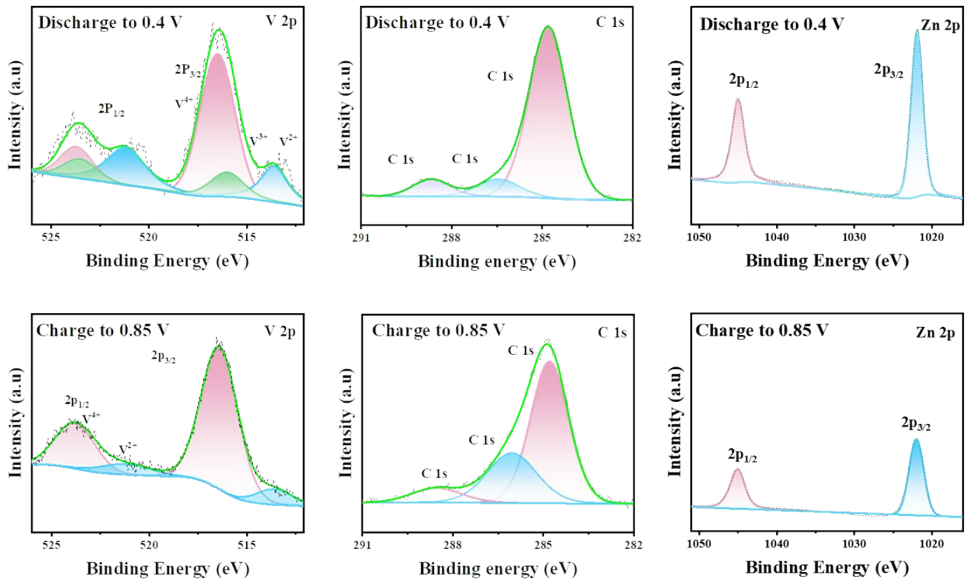

Figure S14. Discharge to 0.4 V and charge to 0.85V high-resolution XPS spectra of Zn 2p, C1s and V 2p.

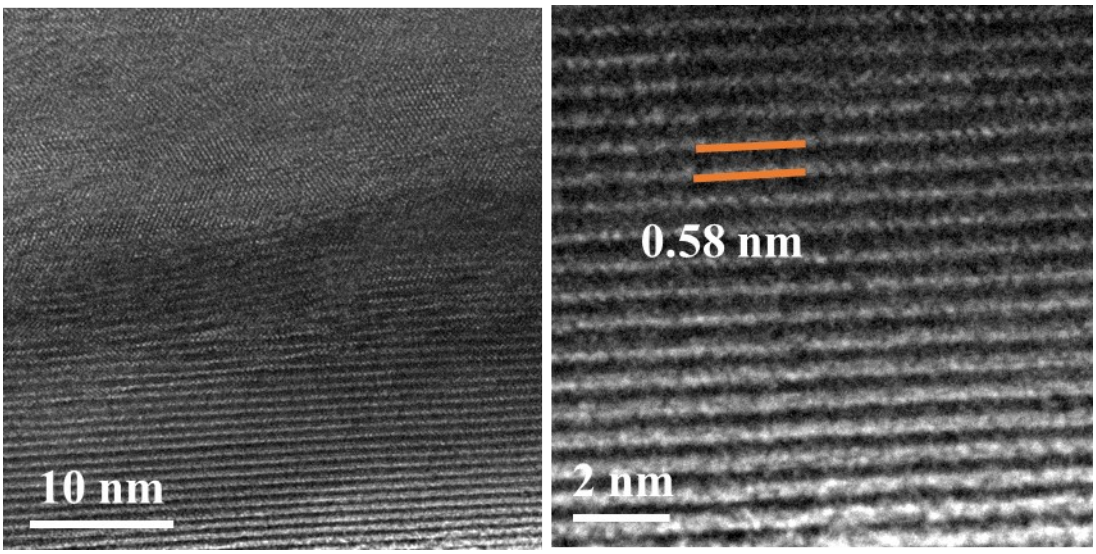

Figure S15. HRTEM micrographs of the (001) crystal plane of C-VS_2@SS before discharge.

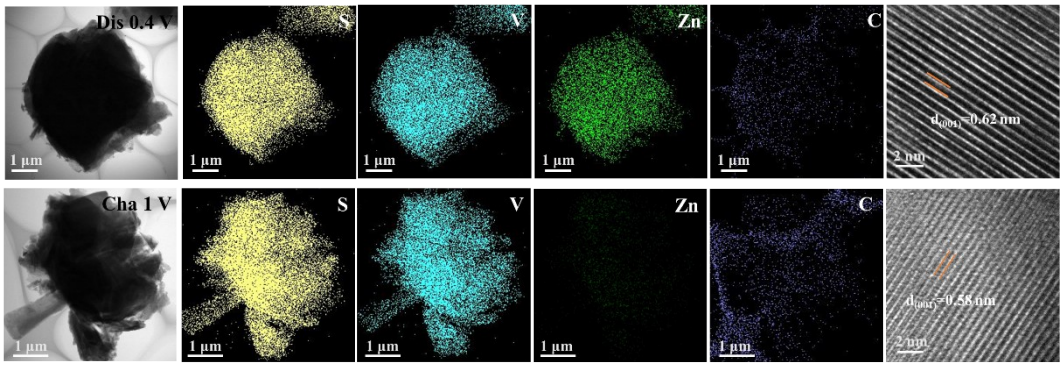

Figure S16. Discharge to 0.4 V and charge to 0.85V ABF-STEM Micrograph, HRTEM Micrograph of the (001) Crystal Plane, and EDS Mapping Images.

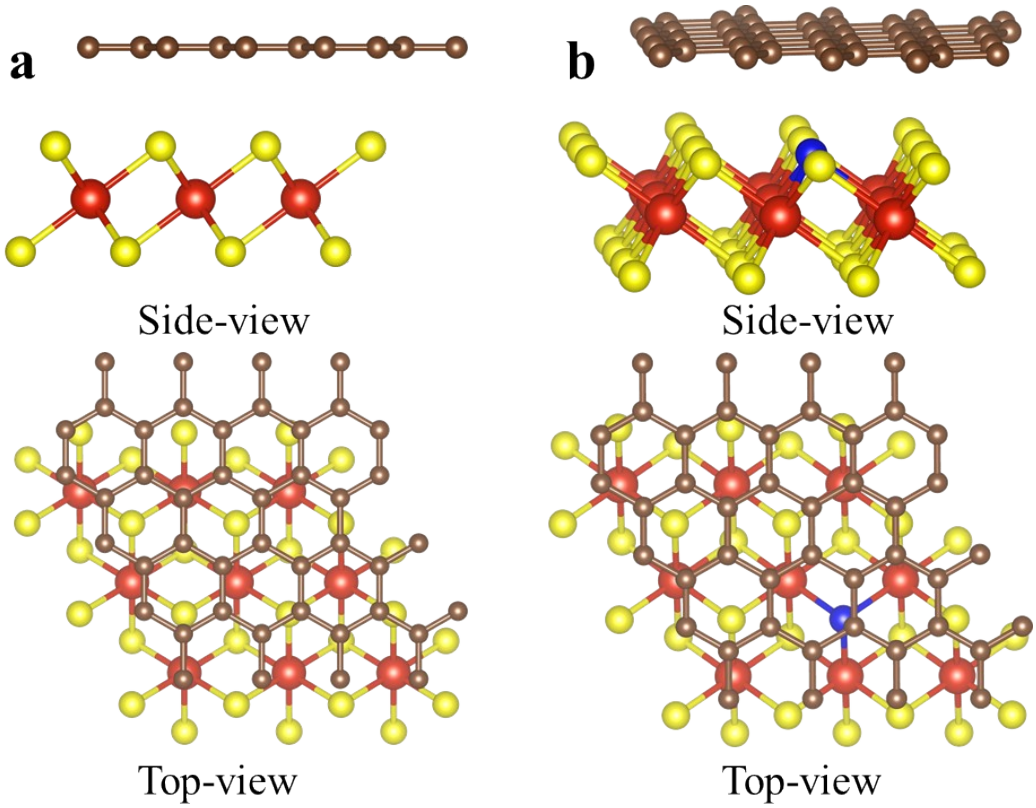

Figure S17. Atomic structure of (a) C-VS_2 and (b) C-VS_2 with V_S defect. (Yellow, red, and gray spheres represent S, V, and C atoms, respectively. The blue sphere represent the S vacancy defect.)

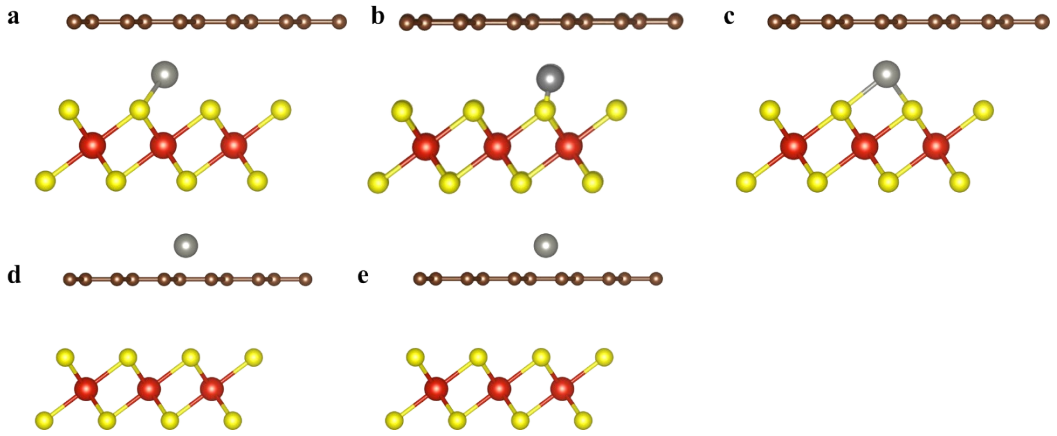

Figure S18. The possible adsorption site of Zn^{2+} on C-VS_2. (a) T_V (Zn atom on top of the V atom), (b) T_S (Zn^{2+} on top of the S atom), (c) T_T site (Zn^{2+} on top of the triazine ring), (d) T_C (Zn^{2+} on top of the C atom) and (e) H_C (Zn^{2+} on top of C layer).

The atomic structure of C-VS_2 with and without S vacancy (V_S) was shown in Fig. S17. The possible adsorption sites of Zn^{2+} in the present study include the T_V (Zn^{2+} on top of the V atom), T_S (Zn^{2+} on top of the S atom), T_T site (Zn^{2+} on top of the triazine ring), T_C (Zn^{2+} on top of the C atom) and H_C (Zn^{2+} on top of C layer), as shown in Fig. S18. The adsorption energy was calculated by the equation $E_{ad} = E_{total} - E_{sub} - E_{Zn}$. E_{total} is the total energy of the system after Zn adsorption. E_{sub} is the energy of the pure substrate without adsorbed Zn. E_{Zn} is the energy of the Zn^{2+}. As shown in Table 1, in the pristine lattice system, the adsorption of the Zn^{2+} exhibits strong site dependence, with the overall interaction being relatively weak. Specifically, the adsorption energy of the Zn^{2+} at the T_S site is positive, indicating that adsorption on top of the surface sulfur atoms is highly thermodynamically unstable. On this intact surface, Zn can achieve stable

adsorption in the interstitial or hollow regions of the lattice, namely at the T_V (-0.383 eV) and T_T (-0.371eV) sites. In the C-VS_2 with V_S defect system, the adsorption energies of the Zn^{2+}across the four candidate sites decrease significantly. The vacancy defect dominates and triggers a highly stable exothermic chemisorption process. Among them, the T_V site exhibits the lowest adsorption energy of -0.564 eV, rendering it the most thermodynamically stable configuration in the entire system. This indicates that the Zn^{2+} will spontaneously seek out and embed into this defect center, forming an exceptionally strong chemical anchor with the exposed underlying transition metal V atom. This demonstrates that sulfur vacancies can significantly enhance the trapping capability and structural stability of the composite material toward Zn^{2+}.

Table S1. Adsorption energy of Zn on C-VS_2 sulfur vacancy (V_S) defect and C-VS_2.

	C-VS_2 with V_S (eV)	C-VS_2 (eV)
T_S	Unstable	Unstable
T_V	-0.564	-0.383
T_T	-0.205	-0.371
T_C	-0.242	-0.108
H_C	-0.252	-0.112

Table S2. The average transferred charge between Zn and substrate was obtained from the Bader charge analysis. The positive value corresponds to gaining charges and the negative value corresponds to losing charges. V_S: sulfur vacancy defect

	C-VS_2 with V_S-Zn (|e|)	C-VS_2-Zn (|e|)
Zn	-1.404	-0.870
V	+0.650	+0.027
S	+0.604	+0.447
C	+0.150	+0.396

Table S3. The electrochemical performances of VS_2 electrode materials.

Materials	Current density(A g^{-1})	Discharge capacity(mAh g^{-1})	Reference
VS_2	0.5	136.80	[6]
VS_2@SS	0.5	168	[7]
Rose D-VS_2	1	186	[8]
VS_2@VOOH	0.5	142.80	[9]
VS_2@N-C	0.5	157.00	[10]
VS_2/CC	0.5	87.00	[11]
VS_2/Mxene	0.5	112.90	[12]
rGO-VS_2	0.5	174.00	[13]
V^{2+}-doped VS_2	0.5	156.30	[14]
VS_2-24	0.5	169.86	[15]
1T-VS_2	2.0	149.50	[16]
VS_2-M	0.5	165.7	[17]
VS_2@CF	0.5	225.32	[18]
VS_2@SWCNT	0.5	167.90	[19]
C-VS_2@SS	0.5	204.3	This work

1. G. Kresse and J. Hafner, *Physical Review B*, 1993, **48**, 13115-13118.
2. G. Kresse and J. Furthmüller, *Physical Review B*, 1996, **54**, 11169-11186.
3. P. E. Blöchl, *Physical Review B*, 1994, **50**, 17953-17979.
4. J. P. Perdew, K. Burke and M. Ernzerhof, *Phys. Rev. Lett.*, 1996, **77**, 3865-3868.
5. S. Grimme, J. Antony, S. Ehrlich and H. Krieg, *The Journal of Chemical Physics*, 2010, **132**, 154104.
6. P. He, M. Yan, G. Zhang, R. Sun, L. Chen, Q. An and L. Mai, *Advanced Energy Materials*, 2017, **7**.
7. T. Jiao, Q. Yang, S. Wu, Z. Wang, D. Chen, D. Shen, B. Liu, J. Cheng, H. Li, L. Ma, C. Zhi and W. Zhang, *Journal of Materials Chemistry A*, 2019, **7**, 16330-16338.
8. T. Li, X. Dong, H. Yang, J. Zhang, R. Huang, Z. Lv, Y. Li, S. Zhang, F. Huang and T. Lin, *Energy & Environmental Science*, 2025, **18**, 3169-3176.
9. X. Pu, T. Song, L. Tang, Y. Tao, T. Cao, Q. Xu, H. Liu, Y. Wang and Y. Xia, *Journal of Power Sources*, 2019, **437**.
10. J. Liu, W. Peng, Y. Li, F. Zhang and X. Fan, *Journal of Materials Chemistry C*, 2021, **9**, 6308-6315.
11. J. Liu, J. Long, Z. Shen, X. Jin, T. Han, T. Si and H. Zhang, *Adv Sci (Weinh)*, 2021, **8**, 2004689.
12. Y. Feng, Y. Feng, Y. Zhang, L. Sun, X. Li, M. Meng, Y. Zhu and K. Liu, *Journal of Power Sources*, 2022, **545**.
13. T. Chen, X. Zhu, X. Chen, Q. Zhang, Y. Li, W. Peng, F. Zhang and X. Fan, *Journal of Power Sources*, 2020, **477**.
14. J. Gao, X. Qi, B. Yang, H. Quan, C. Hu, X.-F. Wang, C. Sun and S. Wang, *Journal of Alloys and Compounds*, 2023, **960**, 170550.
15. S. Zhao, Y. Liu and X. Wu, *CrystEngComm*, 2023, **25**, 1986-1992.
16. Y. Tan, S. Li, X. Zhao, Y. Wang, Q. Shen, X. Qu, Y. Liu and L. Jiao, *Advanced Energy Materials*, 2022, **12**.
17. T. Wang, W. Gao, Y. Zhao, S. Wang and W. Huang, *Journal of Materials Science & Technology*, 2024, **173**, 107-113.
18. Y. Mao, B. Zhao, J. Bai, H. Ma, P. Wang, W. Li, K. Xiao, S. Wang, X. Zhu and Y. Sun, *Small*, 2023, **19**, e2207998.
19. H. Sun, L. Yang, E. Hu, M. Feng, C. Fan, W. Wang, H. Li, X. Wang and Z. Liu, *ACS Appl Mater Interfaces*, 2022, **14**, 40247-40256.